



Boron substitution enhanced activity of $B_xGa_{1-x}As/GaAs$ photocatalyst for water splitting

Xuqiang Zhang^{a,b}, Gongxuan Lu^{b,*}, Xiaofeng Ning^b, Chengwei Wang^{a,*}

^a Key Laboratory of Atomic and Molecular Physics & Functional Materials of Gansu Province, College of Physics & Electronic Engineering, Northwest Normal University, Lanzhou 730070, China

^b State Key Laboratory for Oxo Synthesis and Selective Oxidation, Lanzhou Institute of Chemical Physics, Chinese Academy of Sciences, Lanzhou 730000, China

ARTICLE INFO

Keywords:

Core-shell $B_xGa_{1-x}As/GaAs$ photocatalyst
Boron substitution
Energy barrier of the water dissociation
Heterojunction interface
Built-in electric field

ABSTRACT

Photocatalytic visible water splitting is still impeded by slow kinetics of multi-electron-driven water oxidation, fast carrier recombination and insufficient light absorption of the photocatalyst. Herein, the core-shell heterojunction $B_xGa_{1-x}As/GaAs$ photocatalyst exhibited a remarkably promoted activity for hydrogen generation by direct dissociation of water molecule over boron site on catalyst surface due to redistributing electron density, as well as by promotion of visible absorption and acceleration of charge separation and transfer via a built-in electric field. $B_{0.25}Ga_{0.75}As/GaAs$ photocatalyst exhibited hydrogen evolution rate of 8.4 μmol during 8 h from pure water without electron donor and applied bias.

1. Introduction

Water dissociation on the catalyst surface is important for the photocatalytic water splitting [1,2], photocatalytic environmental cleaning [2,3] and atmospheric chemistry [4]. Although water interactions with photocatalyst can be simplified as dissociative adsorption of the water molecule and form proton (H^+) and OH^- ion [5], the rate and mechanism of photocatalytic hydrogen evolution (PHE) in pure water involves many steps instead [6–9]. Unlike the protons in acidic solution, the high barrier of water molecule dissociation ($K_w = 1 \times 10^{-14}$, 25 °C) leads to slow hydrogen evolution reaction dynamics in most neutral and alkaline catalytic systems [5,10,11]. Overall, water splitting activity is governed not only by the intrinsic ability of the catalyst to catalyze H^+ to H_2 [12,13], but also by the kinetics of H_2O molecule dissociation on the interface [10]. Therefore, promoting the water dissociation is a crucial but challenging step in photocatalytic hydrogen generation.

Water molecule dissociation is an energy uphill process, which need absorb energy or have a strong interaction with host materials [11]. Theoretical researches show that the B atom empty 2p orbitals can be delocalized to the host materials because the B electronic configuration is $2s^2 2p^1$, enhancing the coupling of the lone-pair electrons in the O atom of H_2O molecule with the positive charge center of host materials [11,14,15]. The low electronegativity and small atomic radius of B atom usually lead to a strong covalent character of boron-based compounds

that can enhance interaction with water molecule and facilitate the cleavage of $H-OH$ [16,17]. To understand the H_2O dissociation mechanism and boost the PHE dynamics process, the ternary $B_xGa_{1-x}As$ (x represents the proportion of B in cations) is used as research objects since the amount of boron (B) dopants can be controllable by adjusting the reaction conditions. Moreover, $B_xGa_{1-x}As$ as a crucial and nascent III–V semiconductor is a promising candidate for the top-performing photoelectrochemical water splitting and solar cells due to wide spectral response range, high saturation electron velocity, and stable physical and chemical properties [18,19]. Based on the potential H_2O dissociation effect of the B atoms, the $B_xGa_{1-x}As$ is expected to reduce the activation energy of H_2 formation.

To further solve fast carrier recombination and slow kinetics of multi-charge-driven oxidation in $B_xGa_{1-x}As$ photocatalysts, the construction of p–n junction, element doping, and coupling with co-catalyst have intensively explored [20–23]. Among these methods, interface engineering and spatial arrangements of III–V composite materials, such as core-shell structure, is an effective way to overcome these challenges by designing intimate interfaces and regulating material composition [24–27]. Firstly, the tailorable interface in core-shell catalysts can facilitate the photoexcited carriers separation due to the built-in electric field at heterojunction [24]. Secondly, the core-shell catalysts are more conducive to photon absorption since the spectra of different bands are gradually and repeatedly captured [25]. Thirdly, the stable shell

* Corresponding authors.

E-mail addresses: gxlu@lzb.ac.cn (G. Lu), cwwang@nwnu.edu.cn (C. Wang).

<https://doi.org/10.1016/j.apcatb.2021.120690>

Received 24 May 2021; Received in revised form 25 August 2021; Accepted 3 September 2021

Available online 20 September 2021

0926-3373/© 2021 Elsevier B.V. All rights reserved.

material can provide functional active sites and act as a protective layer, resulting in overall materials surface modification and improving stability [26,27]. Because the suitable bandgap engineering and similar lattice structure perfectly match $B_xGa_{1-x}As$, the narrow bandgap GaAs is usually regarded as ideal core materials to prepare the core-shell $B_xGa_{1-x}As/GaAs$ composite functional materials, which has attracted wide interest in the photocatalytic water splitting [28–31]. Considering

these factors mentioned above, core-shell $B_xGa_{1-x}As/GaAs$ should endow excellent PHE activity due to spontaneous water dissociation, efficient broad spectrum absorption and photogenerated charge separation.

In this work, the core-shell heterojunction $B_xGa_{1-x}As/GaAs$ photocatalyst was synthesized using a solid-phase thermal substitution technology and exhibited a remarkably promoting visible absorption due to

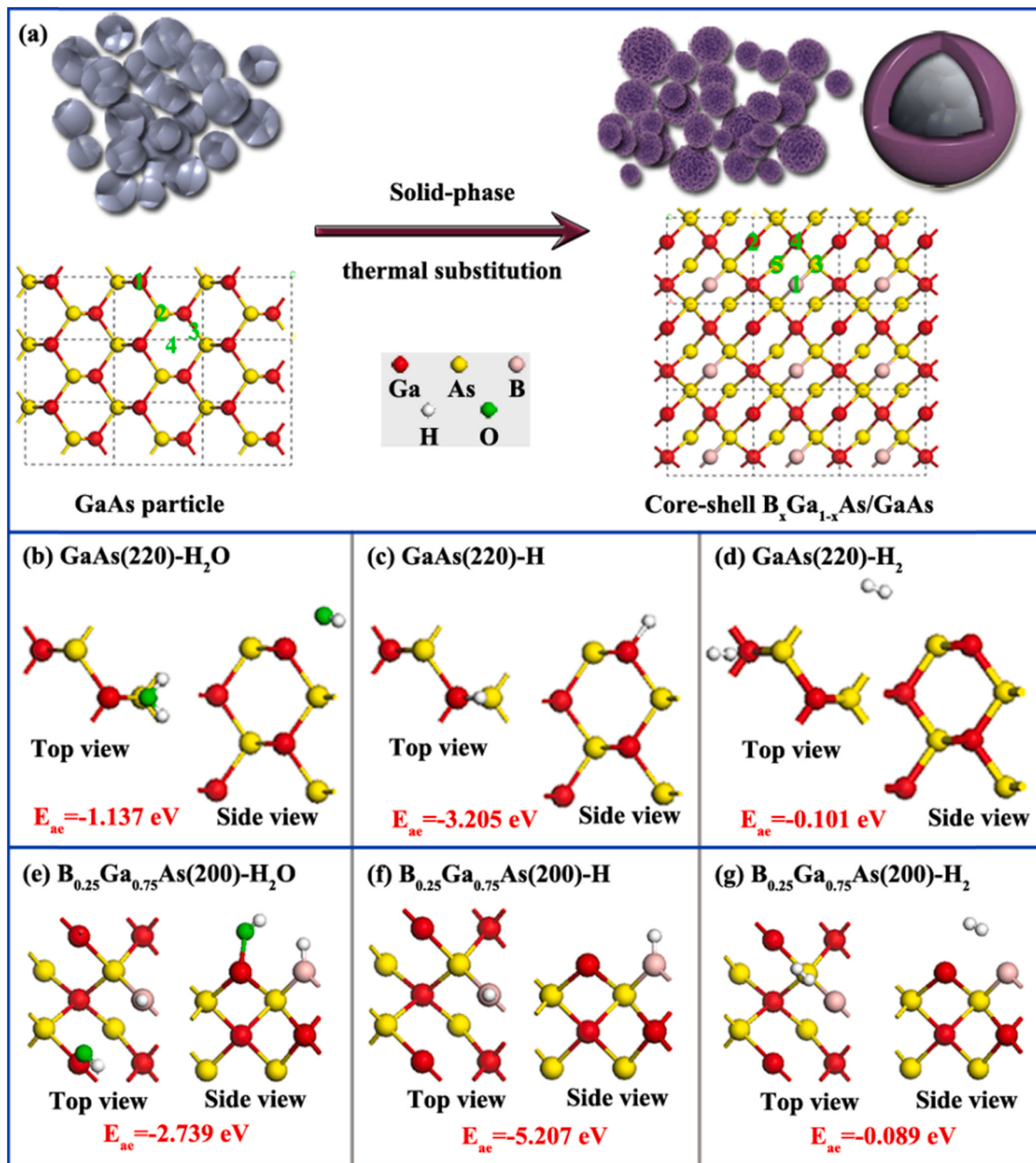


Fig. 1. (a) Schematic illustration on the synthesis of core-shell $B_xGa_{1-x}As/GaAs$ photocatalysts. Optimal adsorption sites for H_2O (b), H (c) and H_2 (d) on the $1 \times 1 \times 1$ supercell of GaAs (220). Optimal adsorption sites for H_2O (e), H (f) and H_2 (g) on the $1 \times 1 \times 1$ supercell of $B_{0.25}Ga_{0.75}As$ (200). The number represents the different adsorption sites before optimization.

assembling of the narrow bandgap core-GaAs (1.31 eV) with the wide bandgap shell-B_{0.25}Ga_{0.75}As (1.58 eV). The photoexcited charge transmission and separation were accelerated due to well matched band structure and an effective built-in electric field between heterojunction interface. The theoretical simulations found that shell-B_{0.25}Ga_{0.75}As was more conducive to reactants adsorption and desorption characteristics than bare GaAs. In particular, the B dopant sites on the catalyst surface can directly dissociate water molecule without external energy due to the electron density redistribution, indicating that the reaction energy barrier of water splitting might be greatly reduced over the B_xGa_{1-x}As/GaAs. As a results, the core-shell B_{0.25}Ga_{0.75}As/GaAs photocatalyst exhibited a high hydrogen evolution activity from pure water without hole scavengers and external bias, achieving hydrogen evolution rate of 8.4 μmol during 8 h irradiation.

2. Experimental section

2.1. Catalysts preparation

GaAs nanoparticles were obtained in our experiment by full grinding commercially available n-type GaAs wafer (Aladdin Industrial Corporation) with an agate mortar. Before grinding, the wafers were cleaned by ultrasonic cleaning in acetone and alcohol for 10 min each step, followed by blowing dry with N₂ gas. To remove the possible oxide layer on the material surface, the cleaned wafers were chemically etched with the H₂SO₄:H₂O₂:H₂O solution at room temperature. Then samples were dipped in an amine sulfide solution for periods and rinsed in deionised water. Based on the obtained GaAs nanoparticles, the core-shell B_xGa_{1-x}As/GaAs nanoparticles were prepared via a solid-phase thermal substitution technology using NaBH₄ as a precursor of B. During the calcination process, active hydrogen and B released from NaBH₄ would react and substitute with the gallium atoms in the framework of GaAs. The specific experimental process was as follows. The GaAs nanoparticles were mixed with NaBH₄, which follow the quality ratio of 1:4 in a quartz annealing boat. To trigger the reaction and guarantee homogeneous mixing, an appropriate amount of absolute ethanol was added dropwise into the mixture. Then the mixture in the tube furnace was heated at 400 °C for 6 h with N₂ protection. Finally, the core-shell sample was gained by repeated washing with deionised H₂O and dried overnight at 60 °C and marked as B_xGa_{1-x}As/GaAs, where x reflected the content of B that can be controlled by adjusting the reaction temperature (200, 300, 400 and 500 °C). The contents of elements in the samples were determined by XPS technology seen in Table S1, such as the sample prepared at 400 °C was marked as B_{0.25}Ga_{0.75}As/GaAs. The schematic illustration of the experimental process was shown in Fig. 1a.

2.2. Photocatalytic hydrogen production tests

The photocatalytic reduction experiments, including the H₂ production rate and stability, apparent quantum efficiency (AQE), isotopes tracer experiments, and solar-to-hydrogen conversion efficiency (STH) of catalysts, were performed in a sealed Pyrex flask with a silicone rubber septum at room temperature, which contained 13.0 cm² effective irradiation area and 170 mL constant volume. To trigger the photocatalytic reactions under the visible light, a Xe lamp (100 mW cm⁻²) combined with a UV-cutoff filter. For example, 60 mg B_xGa_{1-x}As/GaAs and 100 mL deionised H₂O were added to the sealed pyrex flask. The mix solution was sonicated for 5 min to make the powder dispersed. To remove the residual and dissolved O₂ in the sealed Pyrex flask before irradiation, the reaction system was degassed using argon bubbling. The reactor was magnetically stirred to ensure uniform irradiation of the samples throughout the irradiation process. Under visible-light irradiation, the generated gas was analysed using a highly sensitive Agilent 6820 gas chromatography (GC, TCD, 13 × columns, Ar carrier) after every 1 h of illumination to obtain the H₂ production activity.

AQE of photocatalysts was measured under the irradiation of

monochromatic light (430, 490, 550, 590, 630, 730 and 860 nm) and were calculated by 1(1) [32]:

$$\text{AQE}[\%] = \frac{\text{the number of H atoms}}{\text{the number of photons}} \times 100\% \quad 1$$

STH efficiency of photocatalysts was evaluated under visible light irradiation and obtained based on the 2(2) [33]:

$$\text{STH}[\%] = \frac{\text{energy of generation of H}_2 \text{ by water splitting}}{\text{solar energy irradiating the reaction cell}} \times 100\% \quad 2$$

The PHE stability of catalysts was considered under the same reaction vessel and lighting condition. After going through a complete photocatalytic reaction, the reaction system was degassed again using Ar. Then the photocatalytic system was irradiated again. The isotopes tracer experiments of B_xGa_{1-x}As/GaAs were carried out in a downsized reactor to confirm the products of overall water splitting. In this part, the de-ionized H₂O was replaced by high purity D₂O and H₂¹⁸O. The gas composition was analysed using a high sensitivity Gas Chromatography-Mass Spectrometer (GC-MS, TILON-LC-D200 M).

2.3. Theoretical calculations

To elucidate the intrinsic reasons for enhancing PHE activity of the B_xGa_{1-x}As/GaAs photocatalyst, the theoretical simulations using first-principles calculations with projector-augmented-wave pseudopotentials implemented in the Vienna ab-initio simulation package [34–37] are carried out to obtain the adsorption energy (E_{ae}) of H₂O, H and H₂ on the surface of GaAs (220) and B_{0.25}Ga_{0.75}As (200) due to the high exposure ratio of these crystal planes from the XRD results. E_{ae} is calculated according to Eq. (3):

$$E_{ae} = E_{\text{mole/slab}} - (E_{\text{mole}} + E_{\text{slab}}) \quad 3$$

where E_{mole/slab} is the total energy of the base material and adsorbed molecules, E_{mole} and E_{slab} are the energy of free adsorbed molecules and the energy of isolated surfaces [37]. To obtain better long-range vdW interactions, the generalized gradient approximation is used to describe the exchange and correlation potential in the Perdew–Burke–Ernzerhof [35,36]. The energy convergence criterion and tolerance for force convergence are 1.0 × 10⁻³ eV and 0.01 eV/Å to optimize geometry configurations. To avoid interaction between the base material and the adsorbed targets, the vacuum region is at least 10 Å.

Moreover, the morphology and structural characterizations, photoelectric performance tests, and photocatalytic oxygen species tests were stated in the Supporting Information.

3. Results and discussion

3.1. Theoretical simulation for interaction between catalyst and H₂O, H and H₂

We carefully design the typical model of B_xGa_{1-x}As material with partially replaced Ga cation site by B atoms, and the calculation using plane-wave density functional theory method is firstly carried out to obtain the adsorption energy (E_{ae}) of H₂O molecule, H atom and H₂ molecule on GaAs (220) and B_{0.25}Ga_{0.75}As (200) planes due to higher exposed crystal planes in x-ray diffraction (XRD). For the adsorption sites of species on the GaAs (220), there are four nonequivalent sites, that is, on the top of Ga atom (1-site) and As atom (2-site), above the Ga-As bridge (3-site), and the centre of the hexagonal ring (4-site). Fig. S1 presents the stable configurations of the H₂O adsorption on the surface of GaAs (220). The adsorption state of the H₂O molecule at 1-site and 2-site has no change, and the E_{ae} are -0.535 and -0.183 eV, respectively. After optimization, H₂O molecule on the 3-site and 4-site are close to the Ga atom, and the maximum E_{ae} is enhanced to -1.137 eV (Fig. 1b). When the H atom is absorbed on the GaAs (220) surface, the adsorption

of 1-site and 3-site to H has the same stable structure and $E_{\text{ae}} = -3.205$ eV (Fig. 1c), while that with As atom at 2-site is about -3.181 eV. H atom placed on the centre of the hexagonal ring (4-site) is close to Ga atom ($E_{\text{ae}} = -2.476$ eV) after optimization. H_2 molecule is placed in the above four positions, and the stable adsorption structures are shown. H_2 molecule at the 3-site ($E_{\text{ae}} = -0.099$ eV) and 4-site ($E_{\text{ae}} = -0.101$ eV, Fig. 1d) move towards Ga atom after optimization and finally adsorb on the side-on of Ga atom. At 1-site and 2-site positions, the H_2 molecule is adsorbed on Ga ($E_{\text{ae}} = -0.068$ eV) and As ($E_{\text{ae}} = -0.056$ eV) atom by weak van der Waals interaction. Therefore, the GaAs catalyst shows good adsorption energy for reactants and products, which provides a necessary condition for obtaining the photocatalytic water splitting.

There are five nonequivalent sites for the adsorption sites of H_2O , H and H_2 on the $\text{B}_{0.25}\text{Ga}_{0.75}\text{As}$ (200), including on the top of B atom (1-site), upper Ga atom (2-site), upper As atom (3-site), lower Ga atom (4-site) and lower As atom (5-site) in Fig. S2. For the water molecule adsorption on $\text{B}_{0.25}\text{Ga}_{0.75}\text{As}$ (200), there are two stable binding forms. When the H_2O molecule is initially placed in the 3-site and 5-site, they will relax to the side-on of the Ga atom and the corresponding E_{ae} are -0.559 and -0.619 eV. It is noteworthy that H_2O molecule at positions 1-site, 2-site and 4-site can be directly dissociated without applied energy, and the maximum E_{ae} reaches -2.739 eV (Fig. 1e). The dissociative H^+ and OH^- are respectively adsorbed by B and Ga atoms, which provide different reaction sites for photocatalytic hydrogen and oxygen production. When the H atom is on the supercell, the H atom is only fixed to the top of the B ($E_{\text{ae}} = -5.207$ eV) and Ga ($E_{\text{ae}} = -3.490$ eV). B species on the surface are more favourable for proton fixation (Fig. 1f), which is consistent with the H_2O dissociation adsorption. When the H_2 molecule is placed at different positions, the molecule is no obvious position migration after relaxation. There is a weak van der Waals interaction between H_2 and the $\text{B}_{0.25}\text{Ga}_{0.75}\text{As}$ (200) (Fig. 1g), which is conducive to the desorption of catalytic products.

In order to accurately evaluate the coupling effect between the catalyst surface and the system molecules, the (111) lattice plane of catalysts is also selected for the theoretical calculations. The corresponding results in Figs. S3 and S4 clearly indicate that $\text{B}_{0.25}\text{Ga}_{0.75}\text{As}$ /GaAs (111) can also dissociate water molecules and reduce reaction energy barrier. Moreover, the effect of surface size of the supercell on the adsorption behavior of the catalyst has an error of only 0.002 eV (Fig. S5), meaning that the $1 \times 1 \times 1$ supercell meets the required surface size for the adsorption behavior of catalyst surface. On the whole, B dopants on the $\text{B}_{0.25}\text{Ga}_{0.75}\text{As}$ /GaAs surface is more favourable for photocatalytic hydrogen production compared with bare GaAs because $\text{B}_{0.25}\text{Ga}_{0.75}\text{As}$ shows stronger adsorption and desorption ability for the reactants and products, more importantly, the direct dissociation of water molecules and the separation of adsorption sites (H^+ and OH^-).

To further elucidate the influence of shell- $\text{B}_{0.25}\text{Ga}_{0.75}\text{As}$ on the water interaction/dissociation, we analyze the Gibbs free energy profiles regarding the water adsorption and dissociation steps on the GaAs (220) and $\text{B}_{0.25}\text{Ga}_{0.75}\text{As}$ (200) surfaces. The water dissociation on the GaAs (220) surface is relatively difficult due to the higher energy barrier ($\Delta G = -0.143$ eV) compared with the water adsorption step ($\Delta G = -0.210$ eV) (Fig. 2a). For the water interaction/dissociation on the $\text{B}_{0.25}\text{Ga}_{0.75}\text{As}$ (200) surface, the Gibbs free energy of water dissociation is significantly decreased to -1.783 eV, which can advance the water dissociation and therefore promotes the proton formation rate [38]. Moreover, the influence of coverage rate is also considered in the Gibbs free energy of water adsorption and dissociation (Fig. S6). Obviously, the dissociation of water molecules is facile at low the ratio of water molecules to boron atoms ($\text{H}_2\text{O}:\text{B} \leq 1:1$) because of the strong electronic interaction between H_2O molecules and boron atoms on the catalyst surface, which show high Gibbs free energy of water dissociation. However, when the ratio of water molecules to boron atoms reaches to 3:2, water molecules that are not paired with boron atoms could be dissociated by coupling with the cation near the boron atoms, resulting in a decrease in the Gibbs free energy of water dissociation. Fig. 2b shows the electron density difference for the bonding state of H_2O on GaAs (220) and $\text{B}_{0.25}\text{Ga}_{0.75}\text{As}$ (200), where the orange colour indicates electron accumulation and the light green colour represents electron depletion. The increased electron density between H and B atom, O and Ga atom in the $\text{B}_{0.25}\text{Ga}_{0.75}\text{As}$ (200) indicates strong bonding between them. Moreover, the calculated binding energies of H_2O on GaAs (220) and dissociative H_2O on $\text{B}_{0.25}\text{Ga}_{0.75}\text{As}$ (200) are respectively -46.302 and -47.039 eV, which is more energetically favourable and thus further enables the following reactions. These simulation results show that B dopants on the catalyst surface can enhance water adsorption, reduce the energy barrier of water dissociation and provide different reaction sites for photocatalytic H_2 and O_2 production. Thus the $\text{B}_{0.25}\text{Ga}_{0.75}\text{As}$ /GaAs system should show good photocatalytic water splitting activity.

3.2. Experimental evidence for $\text{B}_x\text{Ga}_{1-x}\text{As}$ /GaAs dissociation water

Based on the above theoretical study, we successfully synthesized core-shell $\text{B}_x\text{Ga}_{1-x}\text{As}$ /GaAs catalyst with different B content using a solid-phase thermal substitution technology by precise control of reaction conditions and the corresponding content of elements in the samples see in Table S1. To prove that the $\text{B}_x\text{Ga}_{1-x}\text{As}$ can directly dissociate water and form H^+ and OH^- , we firstly test the cyclic voltammetry in 1 M Na_2SO_4 electrolytes at 1 mV/s scan rate, and the results are shown in Fig. 3. Anodic and cathodic peaks of GaAs electrode appearing at -0.69 and -0.83 V (vs reverse hydrogen electrode (RHE)) indicates the redox reactions occurring surface the electrode. The mechanism is based

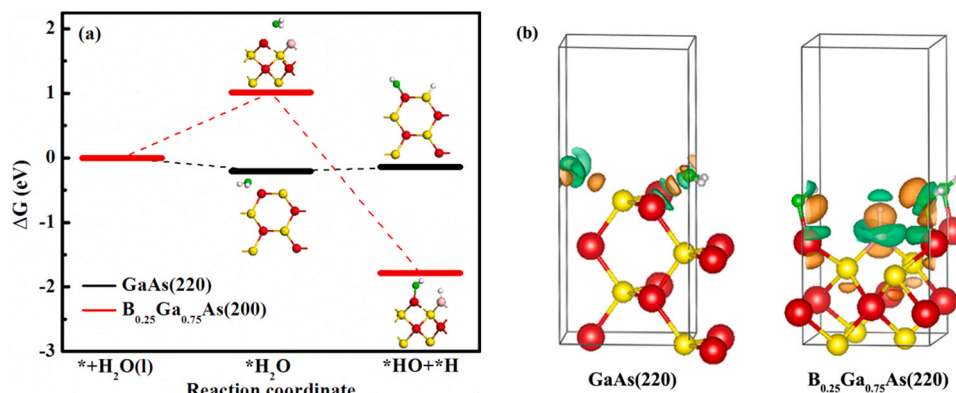


Fig. 2. (a) Density functional theory calculated Gibbs free energy diagram of water adsorption and dissociation on GaAs (220) and $\text{B}_{0.25}\text{Ga}_{0.75}\text{As}$ (200). (b) The electron density difference for the bonding state of H_2O on GaAs (220) and $\text{B}_{0.25}\text{Ga}_{0.75}\text{As}$ (200) with a $0.0042 \text{ e } \text{\AA}^{-3}$ isosurface value. The orange colour represents electron accumulation, and the light green colour represents electron depletion.

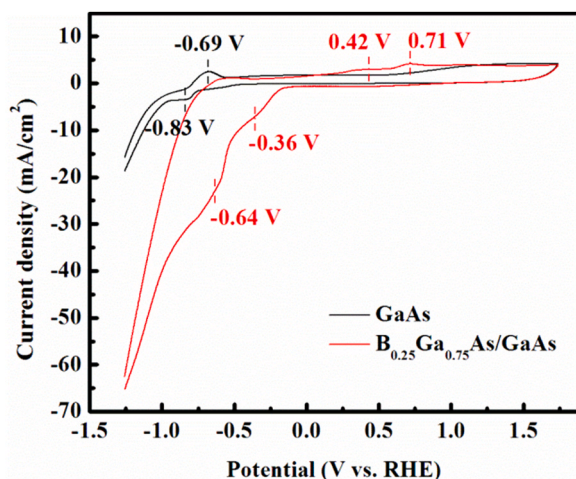


Fig. 3. Cyclic voltammetry of the bare GaAs and $B_{0.25}Ga_{0.75}As/GaAs$ thin films in 0.5 M Na_2SO_4 electrolyte at 1 mV/s scan rates.

on the protons adsorption (or desorption) on the GaAs electrode surface [39]. As observed from the $B_{0.25}Ga_{0.75}As/GaAs$ electrode, there are two sets of redox peaks. A set of peaks are respectively located at 0.71 and -0.64 V vs RHE, similar to the above-mentioned GaAs system. Another set of weaker peaks appear at 0.42 and -0.36 V vs RHE because the OH^- and H^+ produced by the water dissociation on the surface of the catalyst occurs redox reaction under applied bias. The potential difference of the two oxidation peaks and reduction peaks are 0.29 V and 0.28 V, respectively. The similar potential difference means that all the redox reactions on the $B_{0.25}Ga_{0.75}As/GaAs$ electrode surface come from OH^- and H^+ ions. The OH^- and H^+ from directly dissociating water adsorbed on the gallium and B sites can decrease the energy barrier of water splitting, and the corresponding energy barrier is reduced by at least 0.28 eV. This conclusion can be further confirmed by the theoretical simulation of the Gibbs free energy profiles regarding the H^+ and H atom forming H_2 on $B_{0.25}Ga_{0.75}As$ (200) surface (Fig. S7).

3.3. Morphological and structural characterization

Fig. 4a and b are the transmission electron microscopy (TEM) of bare GaAs and $B_{0.25}Ga_{0.75}As/GaAs$, exhibiting a similar particles morphology and size. Bare GaAs has high crystallinity and shows well-resolved lattice features in the high-resolution TEM image (Fig. 4c). After solid-phase thermal treatment at 400 °C, $B_{0.25}Ga_{0.75}As/GaAs$ displays a unique core-shell structure in Fig. 4d. The shell overlay is averagely thickness 5 nm and tightly contacts with a crystalline core GaAs. 0.33 nm of lattice spacing belong to (111) plane of sphalerite in bare GaAs and core GaAs. The elemental mapping images of $B_{0.25}Ga_{0.75}As/GaAs$ (Fig. 4e–h) exhibit that gallium, arsenic and B elemental spots relatively homogeneous, implying the B species are successfully implanted into the sample. To prove the core-shell structure of the composite catalyst, the small-size GaAs wafer is directly thermal treated under exactly the same conditions. The element distribution in the cross-sectional of as-prepared sample clearly show that B signal drops sharply and reaches to zero as the scanning depth increases, indicating that $B_xGa_{1-x}As$ is synthesized and covered on the GaAs surface (Fig. S8). Therefore, combining the HAADF-STEM images and cross-sectional compositional line profiles of $B_xGa_{1-x}As/GaAs$, we can confirm that the composite catalyst synthesized by solid-phase thermal substitution technology has a typical core-shell structure.

From the morphology observation, the surface of $B_{0.25}Ga_{0.75}As/GaAs$ seems to become disordered and show pore structures. Fig. 4i is the N_2 sorption isotherms of samples. Due to the high crystallinity and smooth surface [40], the BET specific surface areas of bare GaAs is only 1.58 m²/g. The formed shell- $B_{0.25}Ga_{0.75}As$ makes the BET specific

surface area of the core-shell catalyst increasing to 7.96 m²/g. Because the catalyst surface disorders after heat treatment, the pore volume of $B_{0.25}Ga_{0.75}As/GaAs$ also increase compared with bare GaAs (Table S2). Moreover, the pore size distribution of core-shell catalyst displays abundant microporous in Fig. 4j, which can provide more transport pathways for reactant and product molecules.

XRD results in Fig. 5a indicate that the samples show a distinct sphalerite phase (JCPDS card 65-0234). The peak intensities and positions of $B_{0.25}Ga_{0.75}As/GaAs$ weaken and shift compared with bare GaAs in Fig. S9, meaning that the solid phase thermal treatment can cause the loss of ordered structures within the GaAs framework. $B_{0.25}Ga_{0.75}As$ overlay is confirmed by two diffraction peaks at 27.92 and 32.32° (Fig. 5b). Since the composition of the ternary $B_xGa_{1-x}As$ is uncertain, there are no definite JCPDS cards to match it so far. Based on the stable $B_{0.25}Ga_{0.75}As$ structure obtained by theoretical simulation in the inset of Fig. 5a, the simulated (111) and (200) crystal plane spacings are 3.199 and 2.769 Å, respectively. According to the Bragg equation [41], the corresponding diffraction angles 2θ are 27.93 and 32.34°. The diffraction angles obtained by XRD experiment and theoretical calculation are very close, confirming the sphalerite phase BGAs. The microstructures of $B_{0.25}Ga_{0.75}As$ are further analyzed by the Raman scattering. Two phonon modes locate at ~ 274 cm⁻¹ (TO) and ~ 297 cm⁻¹ (LO) in samples (Fig. 5c). It shows that the main body of the catalyst is still a sphalerite structure. Compared with the bare GaAs, the two Raman active modes of $B_{0.25}Ga_{0.75}As/GaAs$ shift toward higher wavenumbers. Some researches have verified that the finite size of particles (<10 nm) or elongation of the correlation length owing to the atomic radius can alter phonon vibration energy [29,42]. Herein, the particle size effect is easily eliminated due to the large particle size confirmed with TEM in Fig. 4. The only possibility is the small-radius B dopants resulting in the blue-shift of phonon mode in the core-shell catalyst. These point dopants in many semiconductors can be identified by EPR [43]. A strong EPR signal ($g = 2.004$) with a low hyperfine splitting of 18 G recorded at 140 K can be observed in $B_{0.25}Ga_{0.75}As/GaAs$ sample, while no signal is seen the bare GaAs in Fig. S10.

To further confirm that the core-shell $B_{0.25}Ga_{0.75}As/GaAs$ catalyst is obtained, we study and compare the surface states and chemical composition of samples by X-ray photoelectron spectroscopy (XPS) characterization. The gallium, arsenic, and boron signals are observed in the survey spectra of samples (Fig. S11). From the Ga2p core level XPS spectra of samples in Fig. 5d, the Ga2p_{3/2} peak of $B_{0.25}Ga_{0.75}As/GaAs$ shows higher binding energy than bare GaAs, indicating the B dopants changes the atomic environment of gallium due to its low electronegativity and small atomic radius [42,43]. This result is also verified owing to the shift peak position and shape of the As2p core level in Fig. 5e. Both samples exhibit a peak at 1322.2–1322.6 eV that corresponds to the characteristic peak of As2p-Ga. The additional peak centred at 1325.1 eV in the $B_{0.25}Ga_{0.75}As/GaAs$ is attributed to As2p-B. The B1s core level of core-shell specimen clearly shows a unique peak at 187.6 eV (B1s-As) that originates from the ternary $B_xGa_{1-x}As$ compound (Fig. 5f). A small amount of B1s-Na signal originates from residual pyrolysis products. Therefore, a series of structural characterization can prove that the solid-phase thermal substitution with $NaBH_4$ is an effective and facile method to prepared BGAs film and form a core-shell BGAs/GaAs catalyst. Herein, the core-shell catalysts are beneficial to the repeated absorption of the spectrum and the transfer and separation of photo-generated charges [26,44,45], which provides necessary conditions for photocatalytic water splitting to produce hydrogen.

From the UV–vis–NIR absorption spectra of samples in Fig. 6a, the $B_{0.25}Ga_{0.75}As/GaAs$ shows two special features compared with bare GaAs: a strong response in the whole visible light range and a shoulder absorption at the low-wavelength side. The spectrum absorption comes from core-GaAs. The shoulder absorption can be attributed to the shell parts of the catalyst [46]. According to Tauc's equation [42], the bandgap of the bare GaAs is about 1.31 eV (Fig. 6b). Due to the typical core-shell feature, the $B_{0.25}Ga_{0.75}As/GaAs$ sample exhibits two sets of

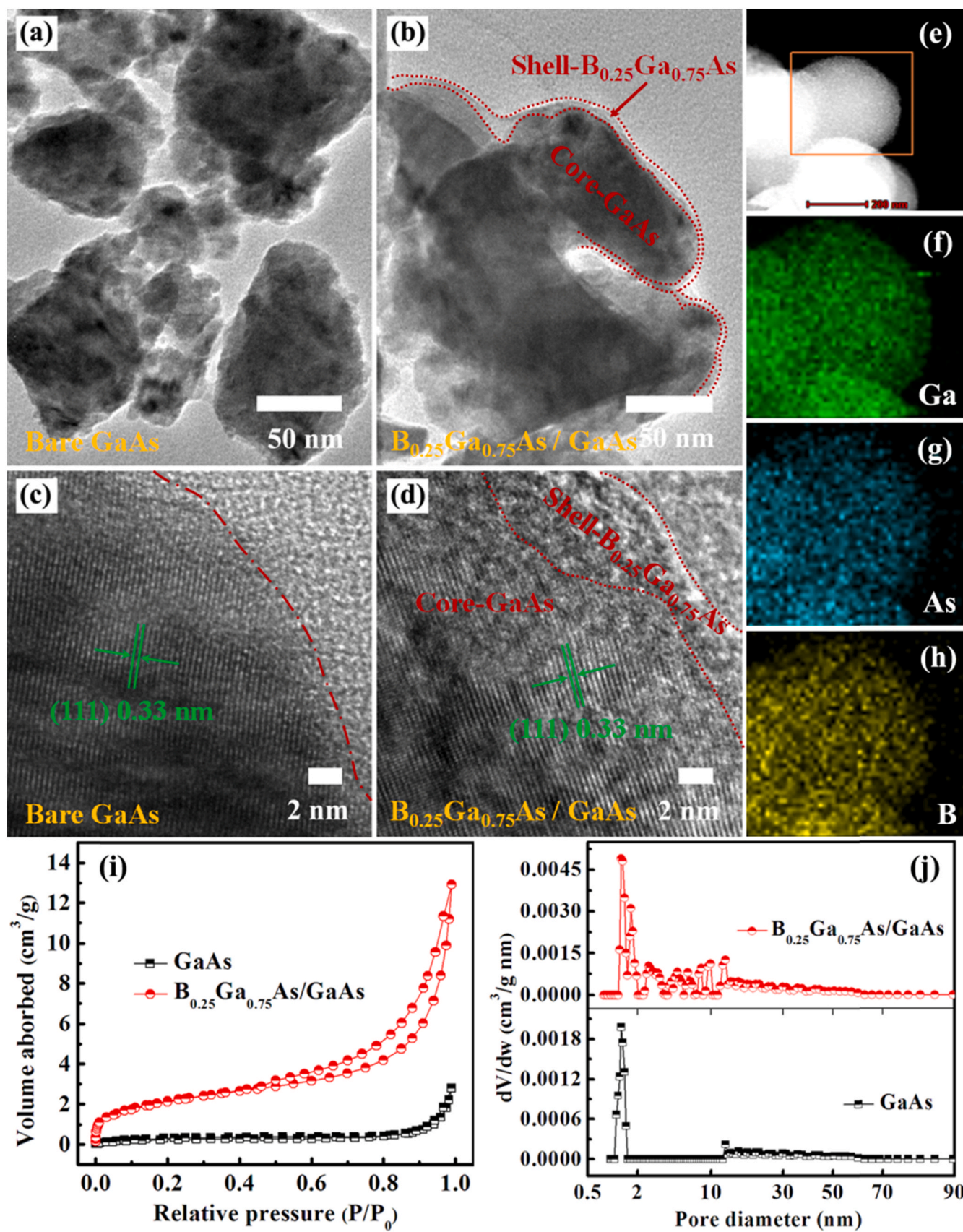


Fig. 4. TEM images of (a) bare GaAs and (b) $B_{0.25}Ga_{0.75}As/GaAs$ with $NaBH_4$ treated at $400^\circ C$; HRTEM images of bare GaAs (c) and $B_{0.25}Ga_{0.75}As/GaAs$ (d). HAADF-STEM images (e) and elemental mapping images Ga (f), As (g) and B (h) of the $B_{0.25}Ga_{0.75}As/GaAs$. (i) N_2 adsorption-desorption isotherms of the catalysts, (j) the corresponding pore size distribution of samples.

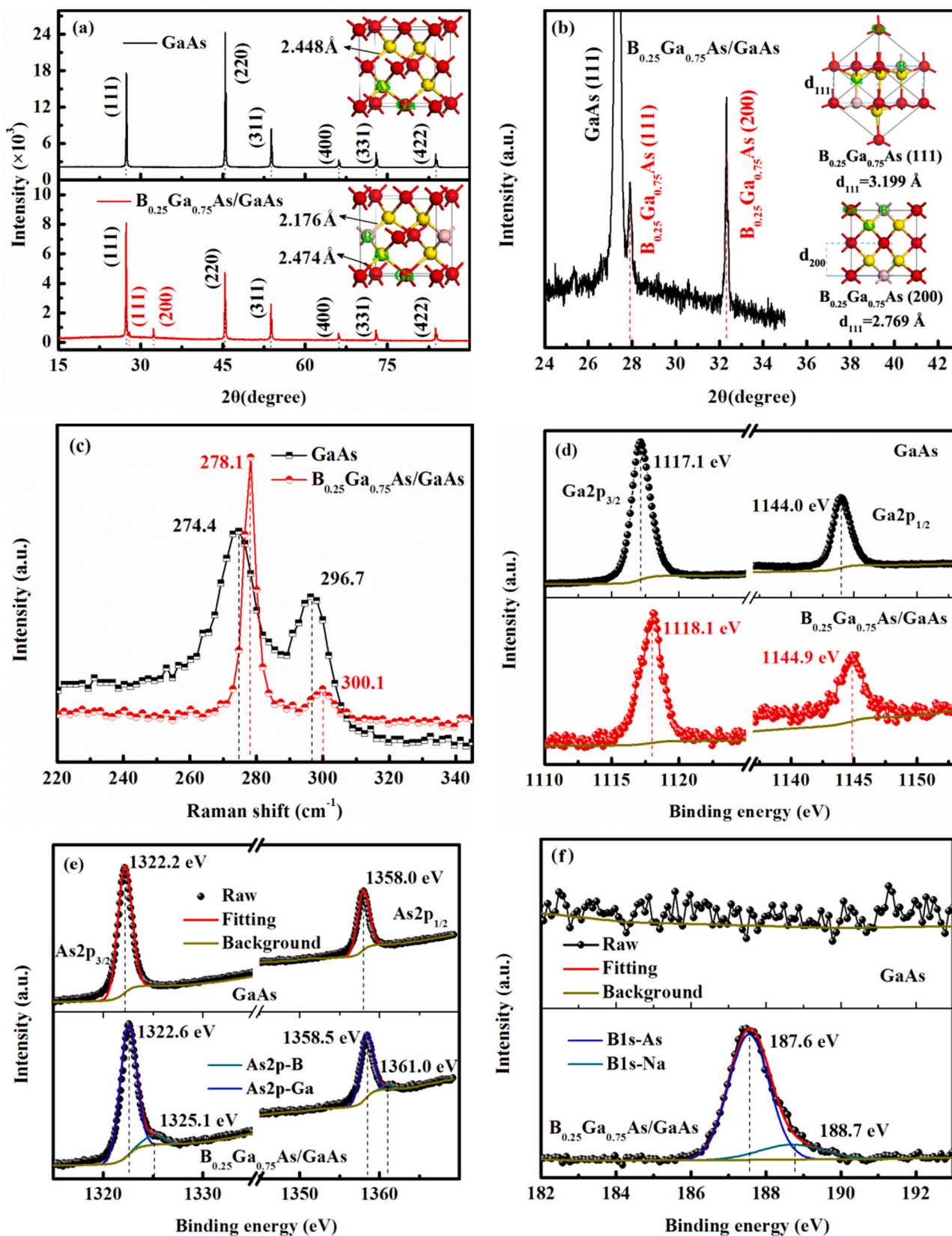


Fig. 5. (a) XRD patterns of bare GaAs and $B_{0.25}Ga_{0.75}As/GaAs$. Inset is the sphalerite crystal structure of GaAs and $B_{0.25}Ga_{0.75}As$. (b) the magnified view of the (111) and (200) crystal face of $B_{0.25}Ga_{0.75}As/GaAs$. Inset: schematic diagram for the (111) and (200) crystal plane spacing of $B_{0.25}Ga_{0.75}As$. Raman spectra (c), high-resolution Ga2p (d), As2p (e) and (f) B1s XPS of the bare GaAs and $B_{0.25}Ga_{0.75}As/GaAs$ specimens.

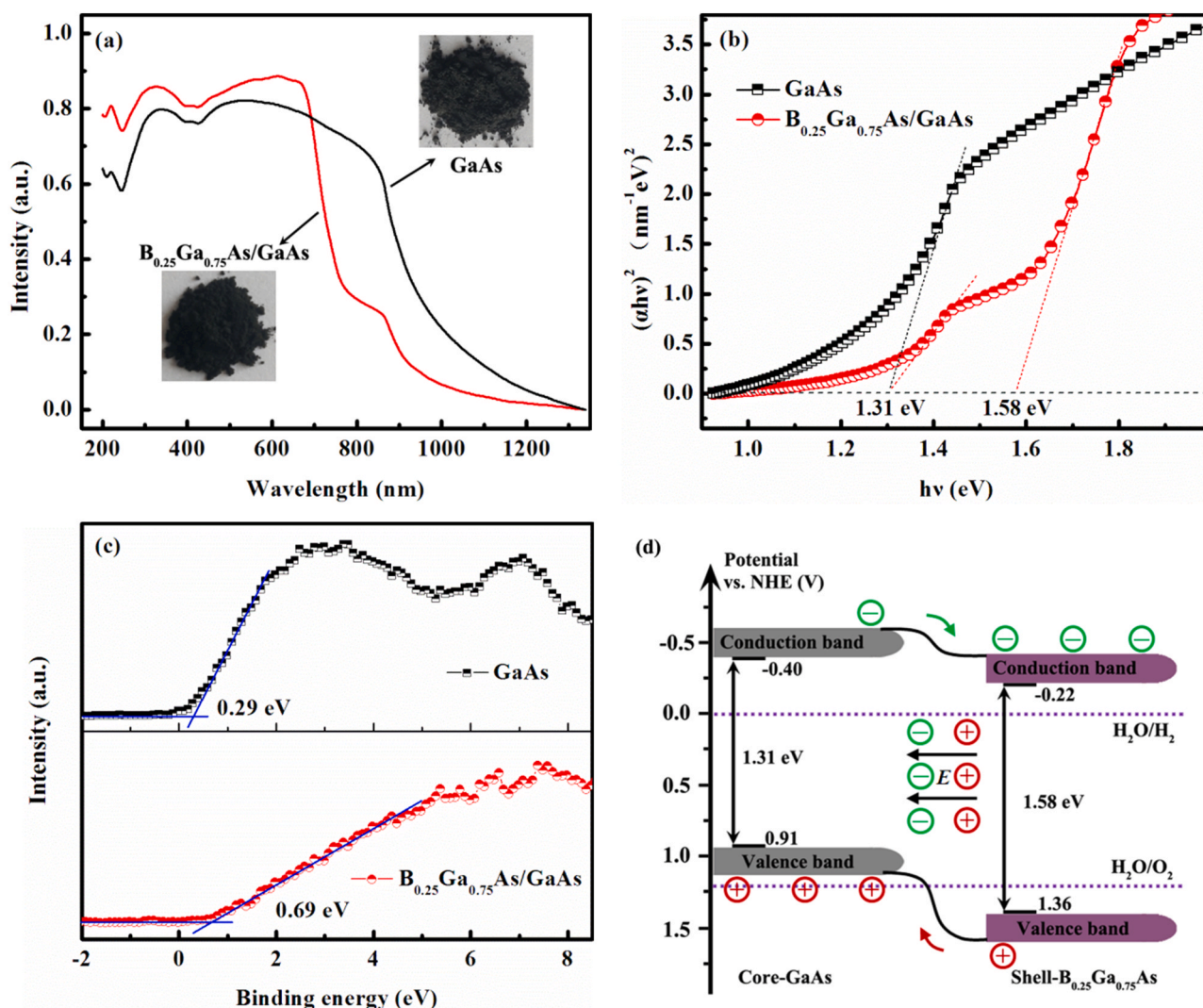


Fig. 6. (a) UV-vis-NIR absorption spectra of bare GaAs and B_{0.25}Ga_{0.75}As/GaAs synthesized at 400 °C with NaBH₄ treatment. (b) Plots of (αhν)² vs (hν) for the corresponding samples. (c) Valence-band XPS spectra of the bare GaAs and B_{0.25}Ga_{0.75}As/GaAs. (d) Band positions and built-in electric field between core-GaAs and shell-B_{0.25}Ga_{0.75}As interface.

simulated band gaps. One is 1.31 eV of core-GaAs, and another is 1.58 eV of shell-B_{0.25}Ga_{0.75}As. Based on the light-absorption features of samples, the core-shell B_{0.25}Ga_{0.75}As/GaAs catalyst should be an active photocatalyst due to the gradual and multiple absorptions of light.

The valence-band XPS spectra and flat-band potential are measured to study the relative band structure of the GaAs-based catalysts. From the valence-band XPS spectra in Fig. 6c, the valence band (VB) energy level of bare GaAs and B_{0.25}Ga_{0.75}As/GaAs are 0.29 and 0.69 eV below the Fermi level. All the samples have typical properties of an n-type semiconductor due to the Mott-Schottky plots exhibit a positive slope in Fig. S12. The flat-band potentials (approximate to the Fermi level) of bare GaAs and B_{0.25}Ga_{0.75}As/GaAs are simulated to be −0.62 and −0.67 V (vs RHE), respectively. According to reported method [47], VB and conduction band (CB) energy levels of catalysts can be simulated by the above bandgap, valence-band XPS spectra and Mott-Schottky plots. The VB and conduction band (CB) energy levels of core-GaAs are estimated to be 0.91 and −0.40 V vs. RHE since the bandgap of bare GaAs and core-GaAs reagent is the same, while the CB and VB energy levels of shell-B_{0.25}Ga_{0.75}As can be calculated to be 1.36 and −0.22 V vs RHE. The VB_{max} and CB_{min} of GaAs is lower than that of B_{0.25}Ga_{0.75}As, which shows a staggered band alignment at the junction of B_{0.25}Ga_{0.75}As/GaAs heterojunction (Fig. 6d). Moreover, the interface between B_{0.25}Ga_{0.75}As and GaAs can form an effective built-in electric field, and its direction

directs from the shell-B_{0.25}Ga_{0.75}As to the core-GaAs. These results suggest that the photogenerated charges will be efficient transferred and separated across the interface. Therefore, the core-shell photocatalyst has a suitable band barrier for charge transport and photon absorption. This is due to perfect band edge positions and reasonable ordering of materials, leading to a better catalytic activity.

3.4. Photoelectric performance test

The time-resolved photoluminescence, I-V test and Hall effect of catalysts are performed at room temperature to evaluate the kinetic process of photogenerated charge migration. Table S3 summarizes the information of fluorescence lifetime τ that is obtained by fitting the decay profiles according to the reported method [48]. Due to expedite the migration of charge carriers and inhibit the electron-hole recombination driven by an effective built-in electric field at the heterojunction interface, the lifetime of B_xGa_{1-x}As/GaAs is significantly higher than bare GaAs (Fig. 7a and Fig. S13). The lifetime of B_xGa_{1-x}As/GaAs gradually prolong with the increase of processing temperature, and the sample prepared at 400 °C shows the longest lifetime ($\tau = 4.52$ ns). The further increase of the reaction temperature reduces the fluorescence lifetime, which may be due to the formed B_xGa_{1-x}As film too thick. The I-V property of the capsules in Fig. 7b is measured by the two-probe

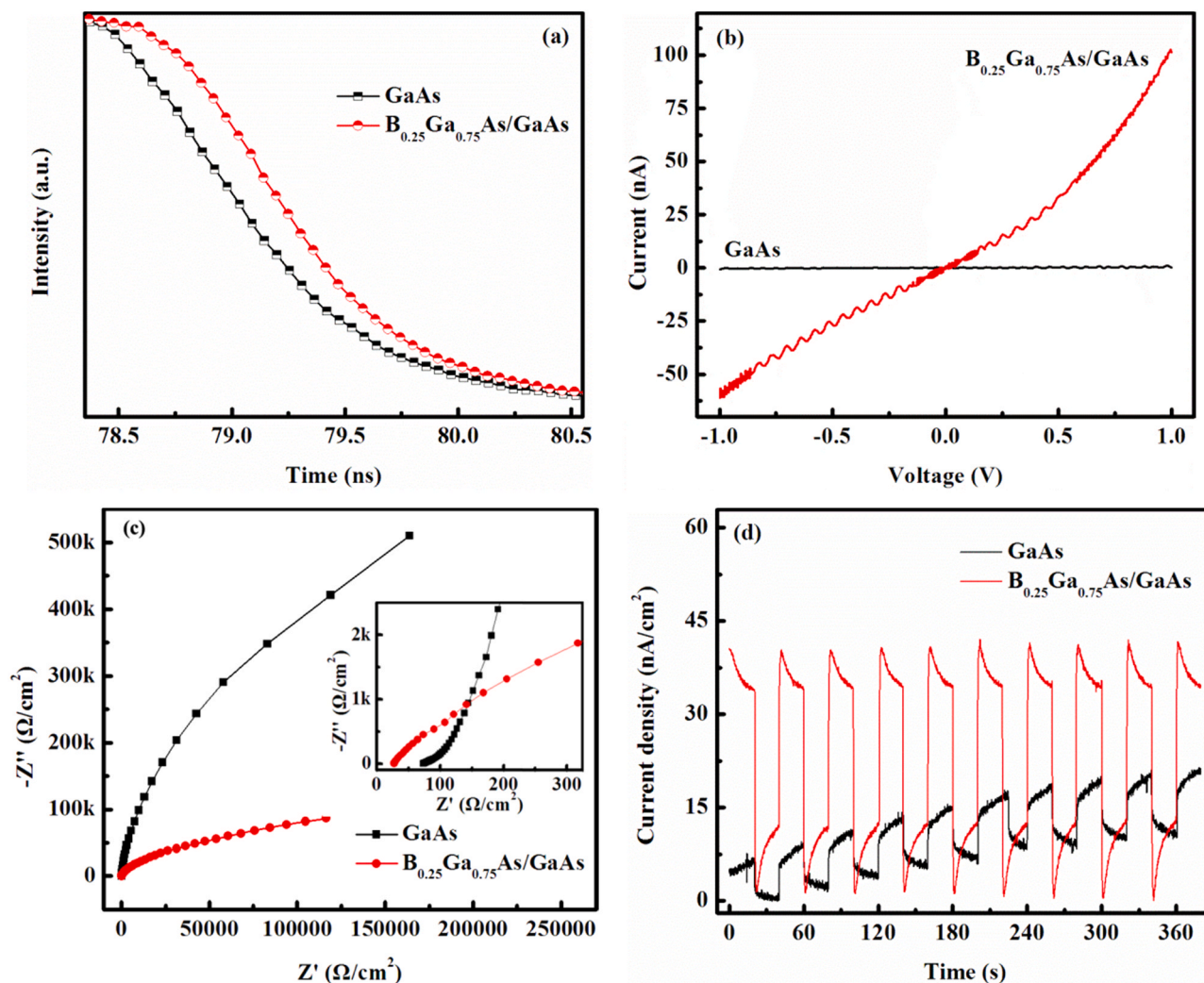


Fig. 7. (a) Time-resolved photoluminescence decay curves, (b) I–V characteristics, (c) Nyquist plots (Inset is the magnified view of Nyquist plots in the high frequency region), and (d) transient photocurrent responses of the bare GaAs and $B_{0.25}Ga_{0.75}As/GaAs$. Electrochemical test in 0.5 M Na_2SO_4 electrolyte.

method, and the $B_{0.25}Ga_{0.75}As/GaAs$ shows a higher current compared with bare GaAs. The I–V curves of $B_xGa_{1-x}As/GaAs$ are unsymmetrical in the voltage sweep range (Fig. S14), meaning the samples possess a typical Schottky barrier since the heterojunction regulates the orientation of electron transmission [29]. The electron transport characteristics of the catalyst are evaluated by the 4-probe Hall measurement, and the corresponding carrier concentration, mobility and resistivity of specimens show in Table 1. All the samples show an n-type behavior that is consistent with Mott-Schottky results. Compared with the bare GaAs, the electrical performances of the $B_xGa_{1-x}As/GaAs$ are greatly improved. Especially for the $B_{0.25}Ga_{0.75}As/GaAs$, the ultrahigh carrier density of $1.17 \times 10^{17} \text{ cm}^{-3}$ and mobility of $8.69 \times 10^2 \text{ cm}^2/\text{V s}$ are mainly

Table 1

Comparison of several electrical parameters extracted from Hall measurement of bare GaAs and $B_xGa_{1-x}As/GaAs$ ($x = 0.03, 0.14, 0.25$ and 0.31). The carrier concentration, mobility and resistivity are denoted as Nb, μ and rho, respectively.

Samples	Nb (cm^{-3})	μ (cm^2/vs)	rho (Ω/cm)
GaAs	-1.14×10^{15}	3.09	1.77×10^3
$B_{0.03}Ga_{0.97}As/GaAs$	-4.01×10^{15}	1.51	1.03×10^3
$B_{0.14}Ga_{0.86}As/GaAs$	-2.18×10^{16}	1.36×10^2	2.11×10^{-1}
$B_{0.25}Ga_{0.75}As/GaAs$	-1.17×10^{17}	8.69×10^2	6.14×10^{-2}
$B_{0.31}Ga_{0.69}As/GaAs$	-9.45×10^{15}	2.81	2.35×10^{-1}

attributable to a lattice-matched heterojunction interface between core-GaAs and shell- $B_{0.25}Ga_{0.75}As$.

The superior charge transfer and separation performances of core-shell catalysts have also been proven through a series of electrochemical characterizations. For example, the Nyquist plot of $B_{0.25}Ga_{0.75}As/GaAs$ electrode shows a small semicircle diameter that means lower transfer resistance in Fig. 7c. The impedance under the high frequency limit value is the internal resistance of the electrode material [49]. As shown in the inset of Fig. 7c, the internal resistance of $B_{0.25}Ga_{0.75}As/GaAs$ electrode is only 28Ω that is lower than the bare GaAs (74Ω), indicating that photogenerated charges are easier to transfer in the composite material. Under the visible light irradiation, the higher transient photocurrent density over core-shell $B_{0.25}Ga_{0.75}As/GaAs$ catalyst means more efficient charge separation than bare GaAs (Fig. 7d). Note that the $B_{0.25}Ga_{0.75}As/GaAs$ electrode shows obvious “peak” in the process of switching between light and dark (Fig. S15) compared with bare GaAs due to the charge trapping effect existing in the carrier transport process inside the device [50,51]. Concretely, when light begins to irradiate the $B_{0.25}Ga_{0.75}As/GaAs$ electrode, the photogenerated exciton at the heterojunction interface are dissociated into electron and hole driven by the built-in electric field, and then transfer to the $B_{0.25}Ga_{0.75}As$ and GaAs respectively. If there is charge trapping traps at the interface, these traps can be effectively filled by free carriers [50,51]. The original built-in electric field between

$\text{B}_{0.25}\text{Ga}_{0.75}\text{As}$ and GaAs is gradually weakened with the filling of the traps, leading to a decrease in the number of carriers collected by the two materials in unit time, so the photocurrent of $\text{B}_{0.25}\text{Ga}_{0.75}\text{As}/\text{GaAs}$ electrode gradually decreases. When the light suddenly stopped, there is a reverse “peak” in the falling process since the interface charge cannot be effectively extracted [52]. Since there is no heterojunction in a single semiconductor, the current variation trends of bare GaAs electrode is different with $\text{B}_{0.25}\text{Ga}_{0.75}\text{As}/\text{GaAs}$. Moreover, in the $\text{B}_{0.25}\text{Ga}_{0.75}\text{As}/\text{GaAs}$ electrode, a drastic increase is observed in the peak currents in the cyclic voltammetry (Fig. 3). These results confirm an enhanced internal charge transfer between $\text{B}_{0.25}\text{Ga}_{0.75}\text{As}$ and GaAs interface in the composite. These observed electrical properties are essential in optoelectronic device applications. Taken together, the core-shell $\text{B}_x\text{Ga}_{1-x}\text{As}/\text{GaAs}$ have all the advantages of high-efficiency photocatalysts, including low energy barrier of water splitting, strong interaction between reactants and photocatalyst, low carrier recombination and sufficient light absorption in the photocatalytic reaction.

3.5. Photocatalytic H_2 evolution from pure water

Under visible light trigger conditions, the PHE experiments of catalysts without any sacrificial reagents are carried out in an air-tight pyrex flask. Take the $\text{B}_{0.25}\text{Ga}_{0.75}\text{As}/\text{GaAs}$ prepared at 400°C as an example; the H_2 , O_2 and N_2 signals are simultaneously found when using the GC to detect the generated gas, but the hydrogen-oxygen ratio not as 2:1. The amount of H_2 increases with the intensity of incident light (Fig. S16), meaning that the obtained H_2 over $\text{B}_{0.25}\text{Ga}_{0.75}\text{As}/\text{GaAs}$ is a typical photocatalytic process rather than a self-corrosion reaction. To further confirm that the core-shell photocatalyst can drive the photocatalytic overall water splitting, the isotopic tracer experiments are performed, and pure water is replaced using D_2O and H_2^{18}O , respectively. The corresponding results in Fig. 8a indicate D_2 ($m/z = 4$) is mainly hydrogen species when D_2O is used, while only a trace of $^{18}\text{O}_2$ ($m/z = 36$) is detected when H_2^{18}O as the target. Approximately equal O_2 signals ($m/z = 32$) in two isotope experiments come from the inevitable pollution in the sampling process. These results indicate that photocatalytic reduction reaction indeed occurs in $\text{B}_{0.25}\text{Ga}_{0.75}\text{As}/\text{GaAs}$ system.

The optimal catalyst concentration is 0.6 mg/mL , meaning the $\text{B}_{0.25}\text{Ga}_{0.75}\text{As}/\text{GaAs}/\text{Pt@Ru}$ catalyst has reached the highest utilisation rate of photons (Fig. S17). Fig. 8b shows the time-dependent H_2 evolution over the catalysts under visible-light irradiation (100 mW cm^{-2} , $\lambda \geq 420\text{ nm}$). In the system of GaAs catalyst, the amount of H_2 is determined to be $0.8\text{ }\mu\text{mol}$ after irradiation 8 h. The core-shell $\text{B}_{0.25}\text{Ga}_{0.75}\text{As}/\text{GaAs}$ exhibits obviously H_2 evolution activity ($8.4\text{ }\mu\text{mol}$), which is around 10-folds improvement compared to the bare GaAs catalyst. Uniformly dispersed co-catalyst Pt and Ru (Fig. S18) as active sites for H_2 and O_2 evolution can further improve catalytic activity, the corresponding PHE activity reach to 3.0 and $14.0\text{ }\mu\text{mol}$ for the GaAs/Pt@Ru and $\text{B}_{0.25}\text{Ga}_{0.75}\text{As}/\text{GaAs}/\text{Pt@Ru}$ under the same conditions. The core-shell catalysts have higher hydrogen evolution activity. By adjusting the reduction temperature from 200 to 500°C , we deeply analyze the influence of the $\text{B}_x\text{Ga}_{1-x}\text{As}/\text{GaAs}$ composition on the catalytic activity to confirm this view (Fig. 8c). Note that the shell- $\text{B}_x\text{Ga}_{1-x}\text{As}$ on the catalyst surface has an irreplaceable effect on the PHE activity.

To further objective evaluation of PHE performance, the AQE of the photocatalysts is measured under monochromatic light irradiation. Overall the AQE of $\text{B}_{0.25}\text{Ga}_{0.75}\text{As}/\text{GaAs}$ is significantly higher than bare GaAs in Fig. S19. The highest AQE of $\text{B}_{0.25}\text{Ga}_{0.75}\text{As}/\text{GaAs}$ is 0.96% at 430 nm irradiation. The AQE at 550 nm is slightly larger than that at 490 nm , the AQE as a whole gradually decreases as the wavelength of monochromatic light increases owing to lower incident photon energy [32,49]. Note that the wavelength-dependent AQE and UV-vis absorption spectrum of $\text{B}_{0.25}\text{Ga}_{0.75}\text{As}/\text{GaAs}$ show an excellent correlation, which further indicates H_2 production originating from the photoexcitation of catalyst (Fig. 8d). STH efficiency is another vital index for

evaluating the catalyst activity. The core-shell catalyst can get about $8.4\text{ }\mu\text{mol}$ of H_2 , and the corresponding solar energy irradiating is 0.8 W , so STH efficiency of $\text{B}_{0.25}\text{Ga}_{0.75}\text{As}/\text{GaAs}$ is $8.6 \times 10^{-3}\%$ in pure water. In addition to extraordinarily PHE activity, the core-shell catalysts also exhibit excellent stability compared with GaAs and GaAs/Pt@Ru (Fig. 8e). The long-term photocatalytic activity of representative $\text{B}_{0.25}\text{Ga}_{0.75}\text{As}/\text{GaAs}$ is maintained well within at least 55 h (Fig. S20). After the photocatalytic reaction, the morphology and element status of catalyst and ion concentration of reaction solution in $\text{B}_{0.25}\text{Ga}_{0.75}\text{As}/\text{GaAs}$ system has no changes compared with untreated samples using TEM, XPS and ICP-OES (Figs. S21–S23). Moreover, the core-shell catalyst also displays good activity in the wide pH range from 3 to 11 (Fig. S24). Overall, the core-shell $\text{B}_x\text{Ga}_{1-x}\text{As}/\text{GaAs}$ photocatalysts exhibit superior PHE activity in pure water.

3.6. Photocatalytic superoxide radical evolution from pure water

All the photocatalytic experiments are executed in pure H_2O without any sacrificial reagents. Since no O_2 is found in all tests, thence, the photogenerated holes must have induced the formation of other oxygen species, such as $\cdot\text{O}_2^-$, $\cdot\text{OH}$ or H_2O_2 . To verify this hypothesis and investigate the leading roles of the active specie, ammonium oxalate (AO), isopropyl alcohol (IPA) and benzoquinone (BQ) as radical scavengers are respectively selected and capture the h^+ , $\cdot\text{O}_2^-$ and $\cdot\text{OH}$ [53]. The steady-state photoluminescence (PL) emission spectra of methyl orange (MO) photoreaction by $\text{B}_{0.25}\text{Ga}_{0.75}\text{As}/\text{GaAs}$ catalyst with radical scavengers show in Fig. S25. Without radical scavengers in $\text{B}_{0.25}\text{Ga}_{0.75}\text{As}/\text{GaAs}$ system, the photoreaction efficiency of MO is 87% because the photo-generated holes directly oxidise pollutants. After adding the AO, BQ and IPA radical scavengers, the MO photoreactions over $\text{B}_{0.25}\text{Ga}_{0.75}\text{As}/\text{GaAs}$ are inhibited, and the corresponding photoreaction efficiency decreases to 81% , 44% and 68% in Fig. 9a. The lowest MO reaction efficiency means that a lot of $\cdot\text{O}_2^-$ radicals can be generated by the light-triggered $\text{B}_{0.25}\text{Ga}_{0.75}\text{As}/\text{GaAs}$ with water and be captured with BQ radical scavenger. The formation of a small amount of $\cdot\text{OH}$ radicals could originate from the complicated chemical reactions of $\cdot\text{O}_2^-$ radicals.

To further confirm the formation of $\cdot\text{O}_2^-$ radicals under illumination, other reagents, hydroxylamine hydrochloride (HH) and safranin T (SFT) as a fluorescent indicator, are also introduced into $\text{B}_{0.25}\text{Ga}_{0.75}\text{As}/\text{GaAs}$ system. Owing to the high oxidation sensitivity between HH and $\cdot\text{O}_2^-$, HH can be oxidized by $\cdot\text{O}_2^-$ radicals and formed nitrite, which further reacts with SFT [54]. As shown in Fig. 9b, a monotonic decrease of the fluorescent signal associated with SFT is found with the increase of the irradiation time, meaning that $\cdot\text{O}_2^-$ radicals gradually increase in this process. However, H_2O_2 is not found in photocatalytic systems because the colour of the reaction solution does not change when o-toluidine and hydrochloric acid is added [55] (Fig. S26). This result is further confirmed by the absorption spectrum of the two-electron oxidised toluidine because the characteristic peak at 438 nm does not appear in the corresponding test of the reaction solution (Fig. S27). All the above experimental results demonstrate that $\cdot\text{O}_2^-$ is the dominant role, while the roles of $\cdot\text{OH}$ and H_2O_2 are minimal in our photocatalytic system. Compared with O_2 production via the four-electron process, the intermediate species easily form because of the two-electron process, which accelerates water oxidation and is conducive to the generation of large-scale electrons and holes for water splitting.

3.7. Photocatalytic water splitting mechanism

Based on experimental results and theoretical simulation, a tentative photocatalytic mechanism over the core-shell $\text{B}_x\text{Ga}_{1-x}\text{As}/\text{GaAs}$ system described as following. H_2O molecular is adsorbed on the active catalytic sites in Fig. 10a (step I). B dopants on the catalyst surface promote the dissociation of water molecules and produce many H^+ and OH^- (4), which are adsorbed on the negatively charged B atoms and the

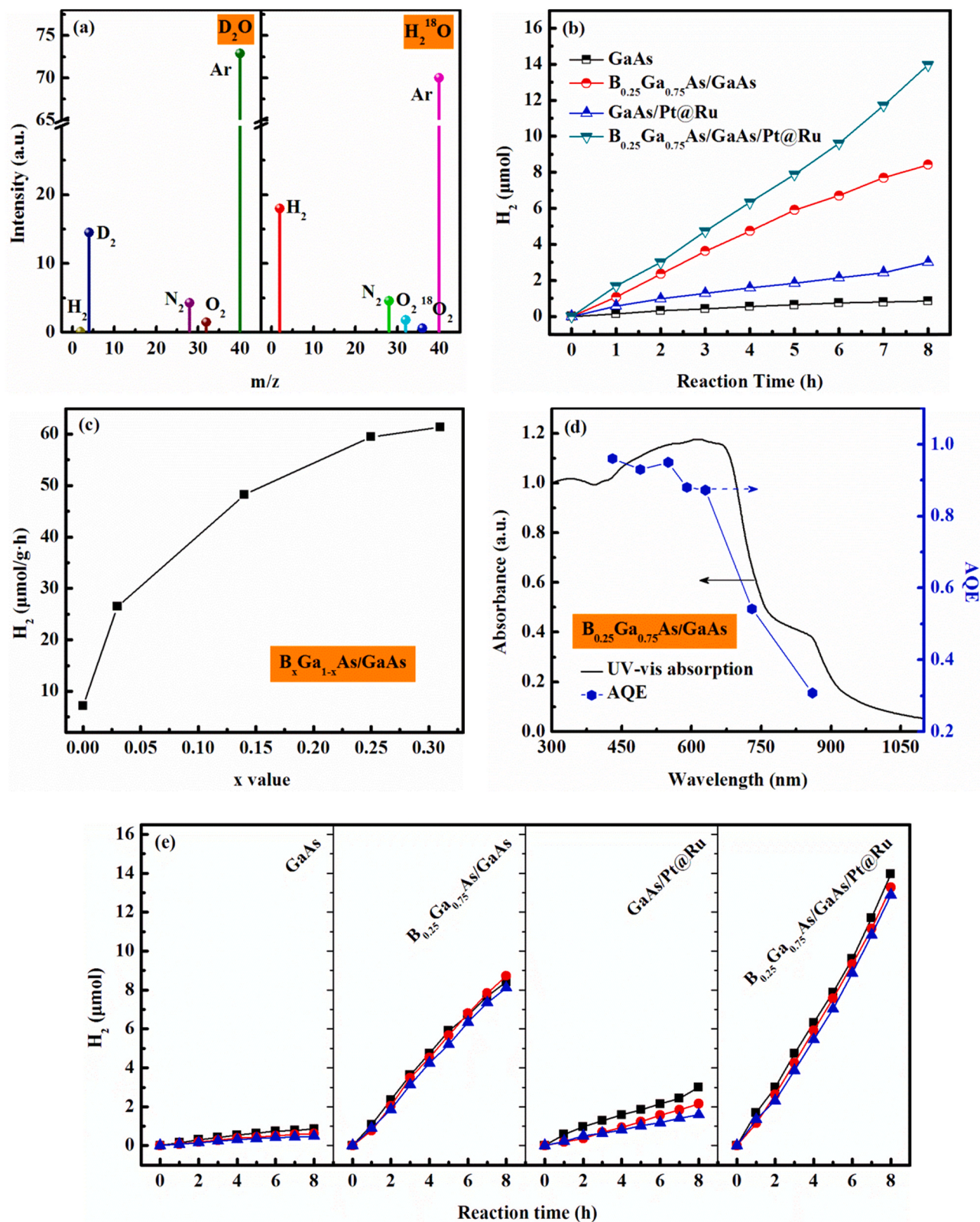


Fig. 8. (a) GC-MS signals of the gas produced by photocatalysis over the $B_{0.25}Ga_{0.75}As/GaAs$ in D_2O and $H_2^{18}O$. (b) Time-dependent H_2 evolution over the $GaAs$, $GaAs/Pt@Ru$, $B_{0.25}Ga_{0.75}As/GaAs$ and $B_{0.25}Ga_{0.75}As/GaAs/Pt@Ru$ catalysts. (c) Effect of B on the photocatalytic activity in the $B_xGa_{1-x}As/GaAs$ catalyst system. (d) UV-vis absorption spectrum and wavelength-dependent AQE of $B_{0.25}Ga_{0.75}As/GaAs$. (e) Stability of PHE over the photocatalysts in pure water.

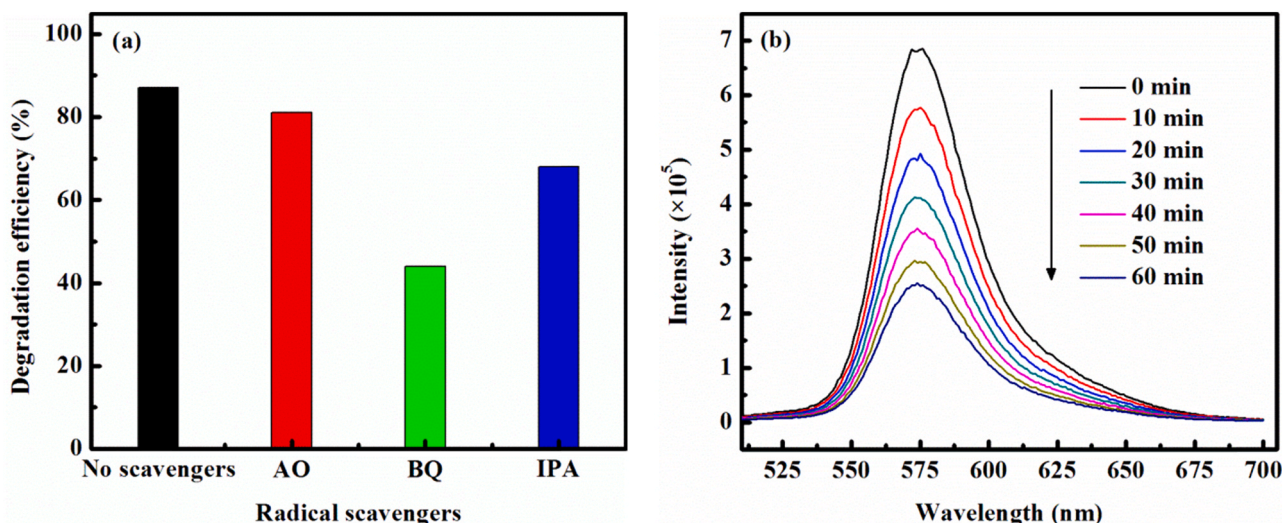


Fig. 9. (a) Effects of radical scavengers on the h^+ , $\cdot O_2^-$ and $\cdot OH$ in the $B_{0.25}Ga_{0.75}As/GaAs$ -MO system. (b) Time-dependent PL emission spectra of the safranin T reacted with formed nitrite that is derived from the oxidation of hydroxylamine hydrochloride with $\cdot O_2^-$.

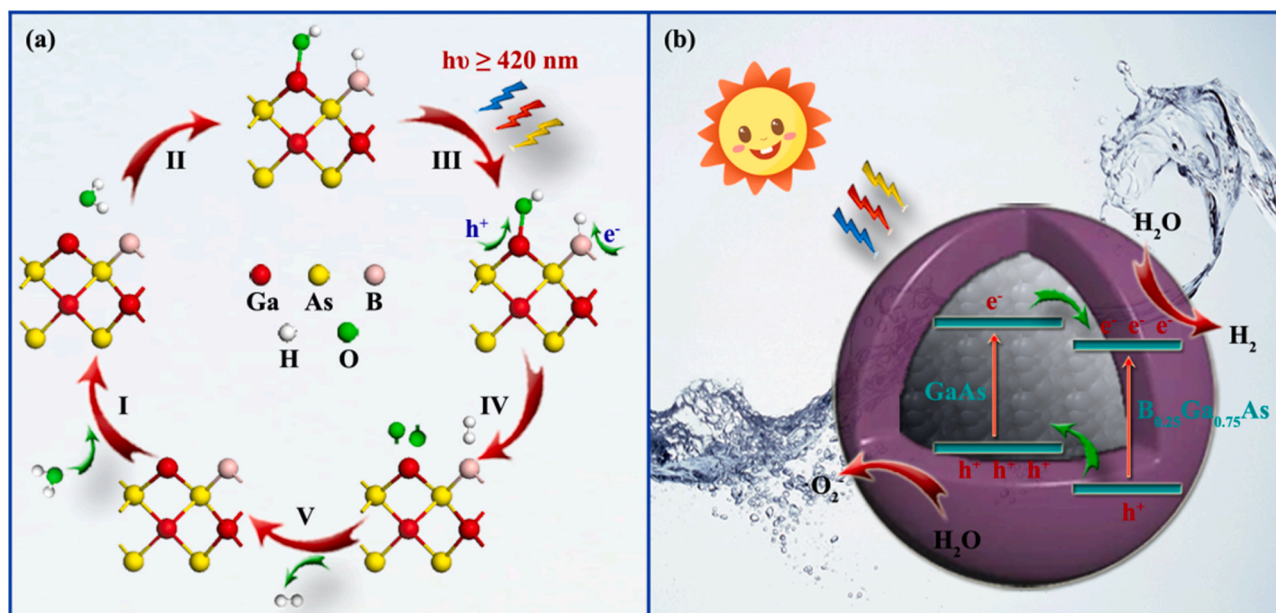
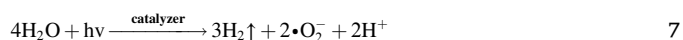
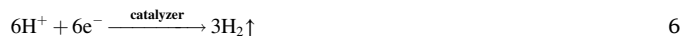
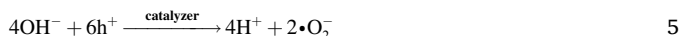


Fig. 10. Schematic diagram: (a) the species evolution over catalyst surface based on hybrid functional first-principles calculations; (b) the mechanism of photocatalytic water splitting for the $B_{0.25}Ga_{0.75}As/GaAs$ photocatalyst under visible light irradiation.

positively charged Ga atoms, respectively (step II). As shown in Fig. 10b, under vis-NIR irradiation conditions ($\lambda \geq 420$ nm), a lot of electron-hole pairs are excited in the core-GaAs and shell- $B_{0.25}Ga_{0.75}As$ because of their relatively narrow band gaps (step III). The photogenerated carriers diffuse to the surface of $B_xGa_{1-x}As/GaAs$ because matching heterojunction interface possesses an effective built-in electric field to accelerate the charge separation [56,57], and then react with adsorbing H^+ and OH^- to form H_2 and $\cdot O_2^-$ radical (5, 6 and step IV). This photocatalytic reaction mechanism could produce excess H^+ ions in the reaction system (7), which is well consistent with the pH value of the solution after irradiation (pH = 4.9) in Fig. S28.



4. Conclusions

Design and synthesis of high-efficient photocatalyst is always a key factor for photocatalytic water splitting using unlimited green solar energy. The high energy barrier of water splitting, the weak interaction between reactants and photocatalyst limit the photocatalytic hydrogen production rate significantly. Moreover, the slow kinetics of multi-charge-driven water oxidation, fast carrier recombination and insufficient light absorption in the photocatalytic reaction also lead to an undesirable solar-to-hydrogen energy conversion efficiency. Herein, the core-shell heterojunction $B_xGa_{1-x}As/GaAs$ photocatalyst synthesized

by a solid-phase thermal substitution technology had addressed these problems simultaneously. A series of structural characterisation and electrical performance tests of catalyst synthesized at 400 °C show that the core-shell $B_{0.25}Ga_{0.75}As/GaAs$ photocatalyst possesses controllable B dopants and a high-quality heterojunction interface, leading to improve photon utilisation efficiency, speed up the transmission and separation of photo-generated charges. The theoretical simulations find that the absorbing water molecules on the core-shell catalyst surface are directly dissociated due to a redistribution of electron density on the $B_{0.25}Ga_{0.75}As$ without any external energy. These positive factors, including the broad spectral absorption, low photogenerated charge recombination, strong water adsorption and low energy barrier of the water dissociation $B_{0.25}Ga_{0.75}As/GaAs$ system, results in an observable photocatalytic activity for hydrogen production in pure water, achieving hydrogen of 8.4 μmol irradiation 8 h and AQE of 0.96% at 430 nm. Although no O_2 is detected in the studied photocatalytic systems, the produced $\cdot O_2^-$ radicals are more conducive to provide a large-scale source of protons and electrons for water reduction because they are formed easily by two-electron process compared to oxygen production via the four-electron process. The superior hydrogen evolution activity of core-shell $B_xGa_{1-x}As/GaAs$ photocatalyst proves its great application potential in solar-driven photocatalytic water splitting. In addition, the results presented here provide a new idea for the design and preparation of high-performance photocatalysts.

CRedit authorship contribution statement

Gongxuan Lu and Chengwei Wang conceived the content and idea of this work, supervised all of the experiments, and revised the paper. Xuqiang Zhang conducted experiments, characterization, analysis, DFT calculation and paper writing. Xiaofeng Ning performed characterization and analysis. All authors contributed to the interpretation of the results and improvement of the paper.

Declaration of Competing Interest

The authors declare that they have no known competing financial interests or personal relationships that could have appeared to influence the work reported in this paper.

Acknowledgements

This work is supported by the China National Key Research and Development Plan Project (No. 2018YFB1502004), the NSF of China (21673262), and LICP Cooperation Foundation for Young Scholars (No. HZJJ20-09).

Appendix A. Supporting information

Supplementary data associated with this article can be found in the online version at [doi:10.1016/j.apcatb.2021.120690](https://doi.org/10.1016/j.apcatb.2021.120690).

References

- N.Z. Koocher, J.M.P. Martinez, A.M. Rappe, Theoretical model of oxidative adsorption of water on a highly reduced reconstructed oxide surface, *J. Phys. Chem. Lett.* 5 (2014) 3408–3414.
- M. Wang, J.T. Ma, G.X. Lu, The inhibition of hydrogen and oxygen recombination reverse reaction on cocatalyst surface in photocatalytic overall water splitting for hydrogen evolution, *J. Mol. Catal. (China)* 33 (2019) 461–485.
- J.D. Baniecki, M. Ishii, K. Kurihara, K. Yamanaka, T. Yano, K. Shinozaki, T. Imada, Y. Kobayashi, Chemisorption of water and carbon dioxide on nanostructured $BaTiO_3$ - $SrTiO_3$ (001) surfaces, *J. Appl. Phys.* 106 (2009), 054109.
- H. Chen, C.E. Nanayakkara, V.H. Grassian, Titanium dioxide photocatalysis in atmospheric chemistry, *Chem. Rev.* 112 (2012) 5919–5948.
- F. Liu, N. Feng, Q. Wang, J. Xu, G. Qi, C. Wang, F. Deng, Transfer channel of photoinduced holes on a TiO_2 surface as revealed by solid-state nuclear magnetic resonance and electron spin resonance spectroscopy, *J. Am. Chem. Soc.* 139 (2017) 10020–10028.
- Y. Jiao, Y. Zheng, K. Davey, S.Z. Qiao, Activity origin and catalyst design principles for electrocatalytic hydrogen evolution on heteroatom-doped graphene, *Nat. Energy* 1 (2016) 16130.
- X.Y. Shi, H.P. Li, H. Zhao, Solid-state Z-scheme photocatalytic systems to splitting water and photo-reduce carbon dioxide, *J. Mol. Catal. (China)* 33 (2019) 391–397.
- H. Jin, X. Liu, Y. Jiao, A. Vasileff, Y. Zheng, S.Z. Qiao, Constructing tunable dual active sites on two-dimensional $C_3N_4@MoN$ hybrid for electrocatalytic hydrogen evolution, *Nano Energy* 53 (2018) 690–697.
- J.H. Ge, Z.P. Zhang, D.C. Jiang, et al., Ni_3N decorated $BiVO_4$ photoanodes for solar-driven water splitting, *J. Mol. Catal. (China)* 35 (2021) 235–242.
- Y. Zheng, Y. Jiao, A. Vasileff, S.Z. Qiao, The hydrogen evolution reaction in alkaline solution: from theory, single crystal models, to practical electrocatalysts, *Angew. Chem. Int. Ed.* 57 (2018) 7568–7579.
- S. Ye, F. Luo, T. Xu, P. Zhang, H. Shi, S. Qin, J. Wu, C. He, X. Ouyang, Q. Zhang, J. Liu, X. Sun, Boosting the alkaline hydrogen evolution of Ru nanoclusters anchored on B/N-doped graphene by accelerating water dissociation, *Nano Energy* 68 (2020), 104301.
- C.C.L. McCrory, S. Jung, I.M. Ferrer, S.M. Chatman, J.C. Peters, T.F. Jaramillo, Benchmarking hydrogen evolving reaction and oxygen evolving reaction electrocatalysts for solar water splitting devices, *J. Am. Chem. Soc.* 137 (2015) 4347–4357.
- N. Logeshwaran, S. Ramakrishnan, S.S. Chandrasekaran, M. Vinothkannan, A. R. Kim, S. Sengodan, D.B. Velusamy, P. Varadhan, J. He, D.J. Yoo, An efficient and durable trifunctional electrocatalyst for zinc–air batteries driven overall water splitting, *Appl. Catal. B: Environ.* 297 (2021), 120405.
- I. Gulyas, R. Kudrawiec, M.A. Wistey, Electronic structure of $BxGa_{1-x}As$ alloys using hybrid functionals, *J. Appl. Phys.* 126 (2019), 095703.
- S. Ilahi, F. Saidi, R. Hamila, N. Yacoubi, H. Maaref, L. Auvray, Shift of the gap energy and thermal conductivity in $BGaAs$ - $GaAs$ alloys, *Phys. B* 421 (2013) 105–109.
- T. Hidouri, M. Biswas, I. Mal, S. Nasr, S. Chakrabarti, D.P. Samajdar, F. Saidi, Engineering of carrier localization in $BGaAs$ SQW for novel intermediate band solar cells: thermal annealing effect, *Sol. Energy* 199 (2020) 183–191.
- T. Hidouri, S. Nasr, I. Mal, D.P. Samajdar, F. Saidi, R. Hamila, H. Maaref, $BGaAs$ strain compensation layer in novel $BGaAs/InGaAs/BGaAs$ heterostructure: exceptional tunability, *Appl. Surf. Sci.* 524 (2020), 146573.
- D. Kang, J.L. Young, H. Lim, W.E. Klein, H. Chen, Y. Xi, B. Gai, T.G. Deutsch, J. Yoon, Printed assemblies of $GaAs$ photoelectrodes with decoupled optical and reactive interfaces for unassisted solar water splitting, *Nat. Energy* 2 (2017) 17043.
- H. Esmaelpour, K.R. Dorman, D.K. Ferry, T.D. Mishima, M.B. Santos, V. R. Whiteside, I.R. Sellers, Exploiting intervalley scattering to harness hot carriers in III-V solar cells, *Nat. Energy* 5 (2020) 336–343.
- S. Han, Y. Li, J. Chai, Z. Wang, Study of the $GaAs/SiH$ van der Waals type-II heterostructure: a high efficiency photocatalyst promoted by a built-in electric field, *Phys. Chem. Chem. Phys.* 22 (2020) 8565–8571.
- H. Sugiura, C. Amano, A. Yamamoto, M. Yamaguchi, Double heterostructure $GaAs$ tunnel junction for a $AlGaAs/GaAs$ tandem solar cell, *Jpn. J. Appl. Phys.* 27 (1988) 269–272.
- C. Bai, T. Hashizume, D. Jeon, T. Sakurai, Geometric and electronic structures of $Na/GaAs$, *J. Vac. Sci. Technol. A* 11 (1993) 525–528.
- K. Choi, K. Kim, I.K. Moon, I. Oh, J. Oh, Evaluation of electrodeless Pt deposition and electron beam Pt evaporation on p- $GaAs$ as a photocathode for hydrogen evolution, *ACS Appl. Energy Mater.* 2 (2019) 770–776.
- Y. Lu, Y. Li, Y. Wang, J. Zhang, Two-photon induced NIR active core-shell structured WO_3/CdS for enhanced solar light photocatalytic performance, *Appl. Catal. B: Environ.* 272 (2020), 118979.
- X. Ning, W. Zhen, X. Zhang, G. Lu, Assembly of ultra-thin NiO layer over $Zn_{1-x}Cd_xS$ for stable visible-light photocatalytic overall water splitting, *ChemSusChem* 12 (2019) 1–12.
- B. Tian, W. Gao, X. Zhang, Y. Wu, G. Lu, Water splitting over core-shell structural nanorod $CdS@Cr_2O_3$ catalyst by inhibition of H_2-O_2 recombination via removing nascent formed oxygen using perfluorodecalin, *Appl. Catal. B Environ.* 221 (2018) 618–625.
- W. Zhen, X. Ning, M. Wang, Y. Wu, G. Lu, Enhancing hydrogen generation via fabricating peroxide decomposition layer over $NiSe/MnO_2$ - CdS catalyst, *J. Catal.* 367 (2018) 269–282.
- X. Zhang, S. Huang, J. Liu, K. Lin, Y. Wang, W. Yang, Research on monolithic $AlGaInP/AlGaInAs/GaInAs/Ge$ quadruple-junction solar cell for high efficiency lattice-matched tandem photovoltaic device, *Appl. Phys. Express* 13 (2020), 071002.
- T. Hidouri, F. Saidi, H. Maaref, Ph Rodriguez, L. Auvray, Localized state exciton model investigation of B-content effect on optical properties of $BGaAs/GaAs$ epilayers grown by MOCVD, *Vacuum* 132 (2016) 10–15.
- D.A. Pryakhin, V.M. Danil'tsev, Y.N. Drozdov, M.N. Drozdov, D.M. Gaponova, A. V. Murel', V.I. Shashkin, S. Rushworth, Growth of $BGaAs$ layers on $GaAs$ substrates by metal-organic vapor-phase epitaxy, *Semiconductors* 39 (2005) 11–13.
- A.J. Ptak, D.A. Beaton, A. Mascarenhas, Growth of $BGaAs$ by molecular-beam epitaxy and the effects of a bismuth surfactant, *J. Cryst. Growth* 351 (2012) 122–125.
- B. Tian, B. Yang, J. Li, Z. Li, W. Zhen, Y. Wu, G. Lu, Water splitting by $CdS/Pt/ WO_3-CeO_2$ photocatalysts with assisting of artificial blood perfluorodecalin, *J. Catal.* 350 (2017) 189–196.
- Q. Wang, T. Hisatomi, Q. Jia, H. Tokudome, M. Zhong, C. Wang, Z. Pan, T. Takata, M. Nakabayashi, N. Shibata, Y. Li, I.D. Sharp, A. Kudo, T. Yamada, K. Domen, Scalable water splitting on particulate photocatalyst sheets with a solar-to-

- hydrogen energy conversion efficiency exceeding 1%, *Nat. Mater.* 15 (2016) 611–617.
- [34] J.P. Perdew, K. Burke, M. Ernzerhof, Generalized gradient approximation made simple, *Phys. Rev. Lett.* 77 (1996) 3865–3868.
- [35] J. Heyd, G.E. Scuseria, M. Ernzerhof, Hybrid functionals based on a screened Coulomb potential, *J. Chem. Phys.* 118 (2003) 8207–8215.
- [36] G. Kresse, J. Furthmüller, Efficient iterative schemes for *ab initio* total-energy calculations using a plane-wave basis set, *Phys. Rev. B* 54 (1996) 11169–11186.
- [37] S. Rondiya, Y. Jadhav, M. Nasane, S. Jadkar, N.Y. Dzade, Interface structure and band alignment of CZTS/CdS heterojunction: an experimental and first-principles DFT investigation, *Mater. (Basel, Switz.)* 12 (2019) 4040.
- [38] M. Yu, D.R. Trinkle, Accurate and efficient algorithm for Bader charge integration, *J. Chem. Phys.* 134 (2011), 064111.
- [39] Z. Lou, J. Xu, J. Zhou, K. Yang, Z. Cao, Y. Li, Y. Liu, L. Lou, X. Xu, Insight into atomic H⁺ generation, H₂ evolution, and cathode potential of MnO₂ induced Pd/Ni foam cathode for electrocatalytic hydrodechlorination, *Chem. Eng. J.* 374 (2019) 211–220.
- [40] J.D. Wang, J.K. Liu, Y. Lu, D.J. Hong, X.H. Yang, Catalytic performance of gold nanoparticles using different crystallinity HAP as carrier materials, *Mater. Res. Bull.* 55 (2014) 190–197.
- [41] Y. Jiang, L. Cao, X. Hu, Z. Ren, C. Zhang, C. Wang, Simulating powder x-ray diffraction patterns of two-dimensional materials, *Inorg. Chem.* 57 (2018) 15123–15132.
- [42] X. Zhang, J. Chen, C. Wang, A. Liao, X. Su, Low-temperature liquid phase reduced TiO₂ nanotube arrays: synergy of morphology manipulation and oxygen vacancy doping for enhancement of field emission, *Nanotechnology* 26 (2015), 175705.
- [43] Y.Q. Jia, H.J. von Bardeleben, A new ESR signal of intrinsic defects in electron-irradiated p-type GaAs, *Phys. Lett. A* 178 (1993) 205–208.
- [44] M. Xing, J. Zhang, F. Chen, B. Tian, An economic method to prepare vacuum activated photocatalysts with high photo-activities and photosensitivities, *Chem. Commun.* 47 (2011) 4947–4949.
- [45] S. Hu, N.S. Lewis, J.W. Ager, J. Yang, J.R. McKone, N.C. Strandwitz, Thin-film materials for the protection of semiconducting photoelectrodes in solar-fuel generators, *J. Phys. Chem. C* 119 (2015) 24201–24228.
- [46] G. Kresse, D. Joubert, From ultrasoft pseudopotentials to the projector augmented-wave method, *Phys. Rev. B* 59 (1999) 1758–1775.
- [47] B. Tian, B. Tian, B. Smith, M.C. Scott, R. Hua, Q. Lei, Y. Tian, Supported black phosphorus nanosheets as hydrogen-evolving photocatalyst achieving 5.4% energy conversion efficiency at 353 K, *Nat. Commun.* 9 (2018) 1397.
- [48] G. Williams, P.V. Kamat, Graphene-semiconductor nanocomposites: excited-state interactions between ZnO nanoparticles and graphene oxide, *Langmuir* 25 (2009) 13869–13873.
- [49] X. Zhang, G. Lu, The spin-orbit coupling induced spin flip and its role in the enhancement of the photocatalytic hydrogen evolution over iodinated graphene oxide, *Carbon* 108 (2016) 215–224.
- [50] I. Hwang, C.R. McNeill, N.C. Greenham, Drift-diffusion modeling of photocurrent transients in bulk heterojunction solar cells, *J. Appl. Phys.* 106 (2009), 094506.
- [51] Q. Liu, M. Yang, J. Zhang, M. Yang, J. Wang, H. Zheng, J. Gou, Three-dimensional dirac semimetal/organic thin film heterojunction photodetector with fast response and high detectivity, *Front. Phys.* 9 (2021), 672591.
- [52] T. Wang, Y. Wang, L. Zhu, L. Lv, Y. Hu, Z. Deng, Q. Cui, Z. Lou, Y. Hou, F. Teng, High sensitivity and fast response sol-gel ZnO electrode buffer layer based organic photodetectors with large linear dynamic range at low operating voltage, *Org. Electron.* 56 (2018) 51–58.
- [53] X. Wang, Y. Li, X. Zhang, J. Lia, X. Li, C. Wang, Design and fabrication of NiS/LaFeO₃ heterostructures for high efficient photodegradation of organic dyes, *Appl. Surf. Sci.* 504 (2020), 144363.
- [54] E.F. Elstner, A. Heupel, Inhibition of nitrite formation from hydroxyl ammonium chloride: a simple assay for superoxide dismutase, *Anal. Biochem.* 70 (1976) 616–620.
- [55] J.H. Liu, Y.W. Zhang, L.H. Lu, G. Wu, W. Chen, Self-regenerated solar-driven photocatalytic water-splitting by urea derived graphitic carbon nitride with platinum nanoparticles, *Chem. Commun.* 48 (2012) 8826–8828.
- [56] X. Ning, G. Lu, Photocorrosion inhibition of CdS-based catalysts for photocatalytic overall water splitting, *Nanoscale* 12 (2020) 1213–1223.
- [57] X. Zhang, G. Lu, Y. Wu, J. Dong, C. Wang, TiO₂ protection layer and well-matched interfaces enhance the stability of Cu₂ZnSnS₄/CdS/TiO₂ for visible light driven water splitting, *Catal. Sci. Technol.* 11 (2021) 5505–5517.